Opto-Electronic Advances

ISSN 2096-4579 CN 51-1781/TN

2D Nb_2CT_x MXene/MoS_2 heterostructure construction for nonlinear optical absorption modulation

Yiduo Wang, Yingwei Wang, Yulan Dong, Li Zhou, Jianlong Kang, Ning Wang, Yejun Li, Xiaoming Yuan, Zhengwei Zhang, Han Huang, Mengqiu Long, Si Xiao and Jun He

Citation: Wang YD, Wang YW, Dong YL, Zhou L, Kang JL et al. 2D Nb_2CT_x MXene/MoS_2 heterostructure construction for nonlinear optical absorption modulation. *Opto-Electron Adv* **6**, 220162(2023).

https://doi.org/10.29026/oea.2023.220162

Received: 9 October 2022; Accepted: 16 February 2023; Published online: 25 April 2023

Opto-Electronic Advances

Article

October 2023, Vol. 6, No. 10

DOI: 10.29026/oea.2023.220162

2D Nb_2CT_x MXene/MoS_2 heterostructure construction for nonlinear optical absorption modulation

Yiduo Wang[1], Yingwei Wang[1]*, Yulan Dong[2], Li Zhou[1], Jianlong Kang[1], Ning Wang[1], Yejun Li[1], Xiaoming Yuan[1], Zhengwei Zhang[1], Han Huang[1], Mengqiu Long[1], Si Xiao[1] and Jun He[1]*

Two-dimensional (2D) nonlinear optical mediums with high and tunable light modulation capability can significantly stimulate the development of ultrathin, compact, and integrated optoelectronics devices and photonic elements. 2D carbides and nitrides of transition metals (MXenes) are a new class of 2D materials with excellent intrinsic and strong light-matter interaction characteristics. However, the current understanding of their photo-physical properties and strategies for improving optical performance is insufficient. To address this issue, we rationally designed and *in situ* synthesized a 2D Nb_2C/MoS_2 heterostructure that outperforms pristine Nb_2C in both linear and nonlinear optical performance. Excellent agreement between experimental and theoretical results demonstrated that the Nb_2C/MoS_2 inherited the preponderance of Nb_2C and MoS_2 in absorption at different wavelengths, resulting in the broadband enhanced optical absorption characteristics. In addition to linear optical modulation, we also achieved stronger near infrared nonlinear optical modulation, with a nonlinear absorption coefficient of Nb_2C/MoS_2 being more than two times that of the pristine Nb_2C. These results were supported by the band alinement model which was determined by the X-ray photoelectron spectroscopy (XPS) experiment and first-principal theory calculation. The presented facile synthesis approach and robust light modulation strategy pave the way for broadband optoelectronic devices and optical modulators.

Keywords: MXenes; optical properties modulation; in situ growth; carriers transfer; nonlinear optical absorption

Wang YD, Wang YW, Dong YL, Zhou L, Kang JL et al. 2D Nb_2CT_x MXene/MoS_2 heterostructure construction for nonlinear optical absorption modulation. *Opto-Electron Adv* **6**, 220162 (2023).

Introduction

Since their discovery in 2004[1], two dimensional (2D) layered materials have been recognized as the foundation of the next generation optoelectronics devices[2] and photonic elements[3] due to their strong and unique light-matter interaction, such as ultrafast and broad optical response in graphene[4], strong excitonic optical properties in single layer transition-metal dichalcogenides (TMDs)[5–7], and tunable direct optical band gap in black phosphorus (BP)[8,9], etc. Recently, a series of newly emerged 2D materials[10–13] have shown interesting nonlinear optical response. In light of remarkable optical properties, 2D layered materials endow new optoelectronics applications that are radically different from their

[1]Hunan Key Laboratory of Nanophotonics and Devices, School of Physics and Electronics, Central South University, Changsha 410083, China; [2]Key Laboratory of Hunan Province for Statistical Learning and Intelligent Computation, School of Mathematics and Statistics, Hunan University of Technology and Business, Changsha 410205, China.

*Correspondence: YW Wang, E-mail: wyw1988@csu.edu.cn; J He, E-mail: junhe@csu.edu.cn

Received: 9 October 2022; Accepted: 16 February 2023; Published online: 25 April 2023

bulk counterparts[14–17].

MXenes are a new family of 2D materials. It can be produced by selective etching methods. Since the first reported Ti_3C_2 MXenes in 2011[18], over 100 kinds of MXenes have been theoretically predicted[19]. They shared a universal formula of $M_{n+1}X_nT_x$, where M is a transitional metal, X represents C/N, and T is the surface termination. Due to the diversity of compositions, MXenes have exhibited tunable and fascinating optical, chemical, and electronic properties, prompting the proposal of the concept of MXetronics[20]. The strong plasmonic feature peaks of different MXenes covering the visible to near-infrared (NIR) spectral range[21,22], resulting in the diversity of photoelectronic[23], photothermal[24], and photovoltaic applications[25]. In terms of their nonlinear optical response, $Ti_3C_2T_x$ thin films were recently reported to have thickness-dependent saturable absorption[26], which was attributed to the plasmon-induced increased ground-state absorption at high optical intensity. In addition, the nonlinear optical absorption response of MXenes has been demonstrated to be modulated by the excitation wavelength[27] and surface group[28], promoting the development of MXenes-based nonlinear optical devices. However, most nonlinear optical research about MXenes is currently focused on reporting the performance or intrinsic properties of a specific MXene. The fundamental understanding of MXenes photo-physics and the strategies for regulating the optical performance of MXenes is still very rudimentary[29].

The strategy for the construction of 2D heterostructure is an important tool for improving the photoelectronic performance of 2D materials-based devices[30–32]. The advantage of each component in 2D heterostructure can be preserved by careful design, and novel properties such as charge transfer or energy transfer between constituents of the 2D heterostructure may appear due to the interfacial effect. Study on the optical response of metal–semiconductor 2D heterostructures is essential for its photodetection and photocatalysis applications[33]. Recently, Nb_2CT_x MXene has been shown to have the highest optical extinction coefficient in the near-infrared region[21]. The few-layer MoS_2 generally demonstrated remarkable optical properties in its excitonic resonance region (~1.8 eV)[34]. Moreover, 2D MXene/MoS_2 heterostructure have shown the great potential for batteries[35,36] and supercapacitor[37], which was attributed to its long-term stability.

Inspired by these advantages, we demonstrated an enhanced linear and nonlinear optical performance of an Nb_2C/MoS_2 heterostructure by *in situ* growing MoS_2 on the surface of Nb_2C nanosheets. Interestingly, the species of surface group in Nb_2C can modulate the work function of Nb_2C/MoS_2, which has been confirmed by X-ray photoelectron spectroscopy (XPS) measurements and density functional theory (DFT) calculation. After comparing the experimental and theoretical results, we determined that the surface group of Nb_2C/MoS_2 was dominated by O termination, leading to the decrease in the work function of Nb_2C after the *in situ* growth of MoS_2. The Nb_2C/MoS_2 inherited the preponderance at a different wavelength of Nb_2C and MoS_2 in absorption and exhibited enhanced broadband optical absorption, which was confirmed by measurement of UV-vis spectrum and DFT calculation. In addition, the saturable absorption of Nb_2C/MoS_2 and pristine Nb_2C was investigated by the Z-scan technique. The nonlinear absorption coefficient and modulation depth of Nb_2C/MoS_2 are greater than those of Nb_2C, but the saturated intensity comparison shows the opposite result. This demonstrates the superior nonlinear optical performance of Nb_2C/MoS_2 to that of Nb_2C. The improved NLO performance can be attributed to the hole transfer from Nb_2C to MoS_2, which caused nonlinear optical response modulation in the heterostructure when combined with the determined energy level alignment. The current findings demonstrated that the Nb_2C/MoS_2 is a promising candidate for high-performance optoelectronic devices and provided an effective method for regulating the nonlinear optical response of MXenes.

Methods

Synthesis of few-layer Nb_2C MXenes

The 2 g Nb_2AlC powder (11 Technology Co., Ltd., China) was added to a 40 mL of 49% HF solution (Macklin Inc.) and stirred for 60 h at room temperature. Then, the excrescent HF solution was washed with water by centrifugation until the pH was close to 6. Subsequently, the washed dispersion was added to the 5% 25 mL TMAOH solution (Macklin Inc.) with stirring for 12 h. The few-layer Nb_2C nanosheets dispersed in water were obtained after washing the excrescent TMAOH.

Preparation of the Nb_2C/MoS_2 heterostructure

The ammonium thiomolybdate (13.3 mg) was added to as prepared Nb_2C nanosheets dispersion (2 mL, 5 mg/mL) and stirred for 12 h until the MoS_4^{2-} was fully

inserted into the surface of the Nb_2C nanosheets in dispersion. Then the precipitate was collected with quick freezing and freeze-drying. After annealing (2 h, 500 °C) in an H_2 (10%)/Ar (90%) atmosphere, we obtained the heterostructure with MoS_2 nanocrystals *in situ* grown on the surface of Nb_2C nanosheets.

Characterization

The TEM, HRTEM, STEM, and element mapping scans were acquired using a Talos™F200X S/TEM (Thermo Fisher Scientific). A BRUKER D8 ADVANCE XRD system was employed for X-ray diffraction (XRD) phase characterizing. A Renishaw InVia Qontor confocal Raman microscope system was employed for collecting Raman spectra. The XPS measurement was performed with the help of a Thermo Scientific ESCALAB Xi+. The optical absorption spectra were characterized with a UV−vis spectrophotometer (UV-2600, Shimadzu).

OA Z-scan system

The nonlinear optical (NLO) absorption was characterized by an open aperture (OA) Z-scan system. A mode-locked Ti: sapphire system operating at 800 nm with 35 fs pulses at a 2 kHz repetition rate and a TOPAS (Light-Conversion) optical parametric amplifier was employed as a laser source. The Z-scan system measures the transmittance of the sample as a function of optical intensity, where the focal length of lens is 175 mm and beam waist is determined to be 24 μm. The signal was collected with the average power of the optical detectors (OPHIR, PD300 IR).

DFT calculations

The first-principles calculations of Nb_2C/MoS_2 heterostructure were performed by density functional theory as implemented in the Vienna ab initio Simulation Package (VASP)[38] with the projector augmented wave (PAW) pseudopotentials. The generalized gradient approximation (GGA) of Perdew-Burke-Ernzerhof (PBE) functional was used. The plane-wave energy cutoff was set to 500 eV with a precision force of 0.01 eV/Å (1Å=10^{-10} m). The Brillouin zone was sampled with a 9×9×1 k-mesh point setting, and a denser k-mesh 15×15×1 was used for optical properties computations. The vdW interaction was treated with the semi-empirical D2 method (Grimme method). The absorbance $A(\omega)$ was determined by the 2D optical conductivity for low-dimensional systems[39,40]. For the calculations of the Nb atom, the Hubbard U method was employed to treat strong correlation effects, and the U value of the Nb d orbital was set to 6.5 eV[41].

Results and discussion

At first, the few-layer Nb_2C nanosheets are synthesized with selective HF etching and intercalation methods[27]. The synthesis route of Nb_2C/MoS_2 heterostructure is shown in Fig. 1(a). Briefly, the MoS_4^{2-} was inserted into the surface of Nb_2C nanosheets during dispersion. MoS_2 nanocrystals were grown *in situ* on the surface of Nb_2C nanosheets after freeze-drying and annealing in an H_2 atmosphere. Fig. 1(b) and Fig. S1(a) illustrate the transmission electron microscopy (TEM) image of Nb_2C/MoS_2, indicating a uniform, transparent flake structure of Nb_2C/MoS_2. The elemental mapping images were shown in Fig. 1(c). The Nb, Mo, and S elements overlap very well, indicating that the MoS_2 and Nb_2C are integrated very well in a single flake. To further characterize the morphology of MoS_2 on the Nb_2C sheets, high-resolution transmission electron microscopy (HRTEM) was performed (Fig. 1(d) and Fig. S1(b)). The surface of the Nb_2C sheet has a clear lattice fringe. After careful measurement, the interplanar crystal spacing was determined to be 0.62 nm, which agrees well with the d-spacing of the (002) plane in MoS_2. The selected area electron diffraction (SAED) pattern of Nb_2C/MoS_2 (Fig. 1(e)) matched well with (002) and (103) planes for Nb_2C, (100) and (110) planes for MoS_2, indicating a good overlap of the Nb_2C and MoS_2.

The Raman spectroscopy analysis of Nb_2C/MoS_2 heterostructure is illustrated in Fig. 1(f). The prominent peaks appeared at 218 cm^{-1} and 255 cm^{-1} are attributed to the vibration mode of E^2_{2g} and A_{1g} of Nb_2C[42], respectively, and the peaks located at 378 cm^{-1} and 402 cm^{-1} were assigned to the vibration mode of E^1_{2g} and A_{1g} in MoS_2[43], indicating the successful combination of Nb_2C and MoS_2. X-ray diffraction (XRD) was performed to further characterize the structure of Nb_2C/MoS_2. When compared to the XRD pattern of Nb_2AlC (JCDS PDF#30-0033), the (002) peak of Nb_2C downshifts and broadens to $2\theta = 7.1°$, demonstrating a successful exfoliation of 2D Nb_2C[27]. For Nb_2C/MoS_2 heterostructure, the peaks located at 14.2°, 33.4°, and 58.7° were attributed to the (002), (101), and (110) planes of MoS_2 (JCDS PDF#37-1492), and the signal at 8.7° can be ascribed to the (002) plane of Nb_2C. Because the (002) peak of MXene represents the interlayer spacing, the downshifting of the (002) peak in Nb_2C indicates decreased layer

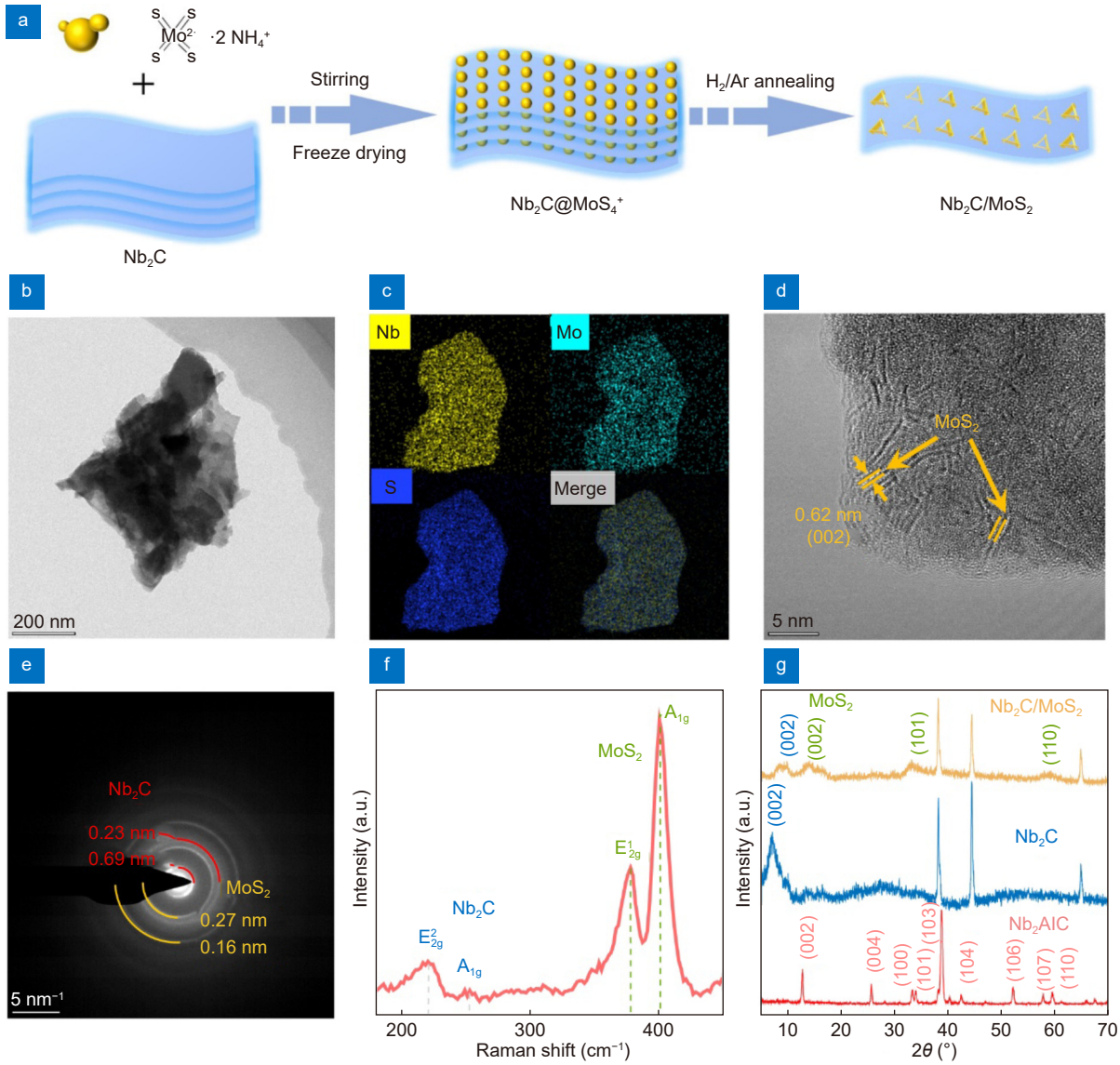

Fig. 1 | Characterization of the Nb_2C/MoS_2 heterostructure. (**a**) Schematic illustration of the *in situ* synthesis of the Nb_2C/MoS_2. (**b**) Transmission electron microscope (TEM) image of Nb_2C/MoS_2. (**c**) Elemental mapping images of Nb_2C/MoS_2, upper left plane: Nb (yellow), upper right plane: Mo (cyan), left lower plane: S (blue), and right lower plane Merge. (**d**) High-resolution transmission electron microscopy (HRTEM) of Nb_2C/MoS_2. (**e**) Selected area electron diffraction (SAED) pattern of Nb_2C/MoS_2. (**f**) Raman spectra of Nb_2C/MoS_2. (**g**) XRD pattern of Nb_2C/MoS_2, Nb_2C, and Nb_2AlC.

spacing after combing with MoS_2.

To analyze the bonding and chemical composition, X-ray photoelectron spectroscopy (XPS) of Nb_2C and Nb_2C/MoS_2 was performed. In the XPS survey pattern spectrum (Fig. S1), the peaks of Nb_2C matched well with Nb, C, O, and F elements, which were presented in the XPS spectrum of Nb_2C/MoS_2. Furthermore, the additional peaks can be found in the Nb_2C/MoS_2 spectrum, which were identified as the feature of Mo and S elements. The C 1s peaks of Nb_2C/MoS_2 (Fig. 2(a) upper plane) consist of three components. The peaks at 284.8 eV, 286.2 eV, and 288.9 eV were designated to sp^3 C-C bond[44], C-O bond[45], and O-C=O bond[45], respectively. As compared to the results shown in Fig. 2(a) (lower plane), the C bonding properties are nearly unchanged after combing with MoS_2 because the position and intensity of the three peaks do not change. In the Nb 3d spectrum (Fig. 3(b) upper plane), the peaks at 207.5 eV and 210.2 eV are related to the $3d_{5/2}$ and $3d_{3/2}$ orbits of Nb atom[46], respectively, which could be assigned to the Nb_2O_5 component[47,48]. In comparison, the peaks of the same components in pristine Nb_2C are downshifted to 206.8 eV and 209.5 eV, and the ratio of the two components does not change (Fig. 2(b) lower plane). These results indicate that the chemical environment of Nb atoms has changed due to the growth of MoS_2, but the valence state of Nb

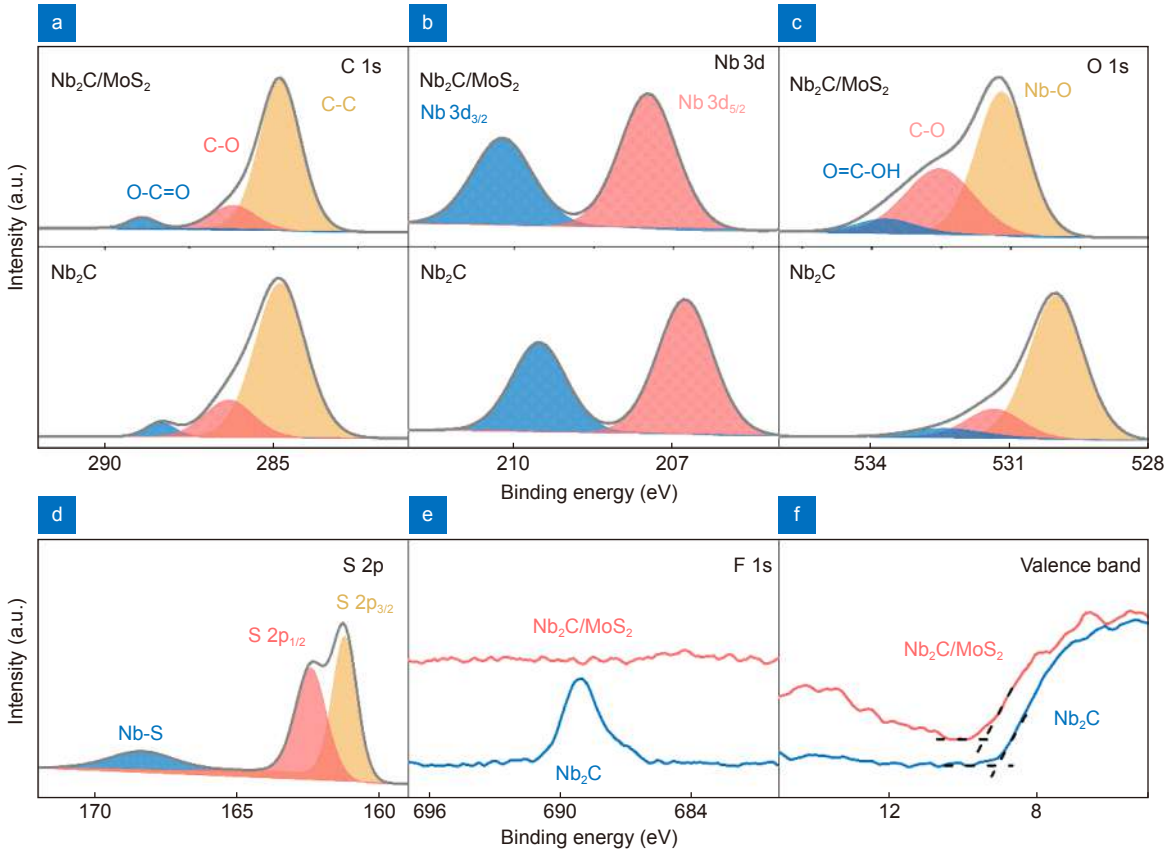

Fig. 2 | XPS spectra of the Nb_2C/MoS_2 and Nb_2C: (**a**) C 1s, (**b**) Nb 3d, (**c**) O 1s, (**d**) S 2p, (**e**) F 1s, and (**f**) valence band.

atoms has not changed. The upper plane of Fig. 2(c) shows the O 1s high-resolution spectrum, which revealed three peaks in Nb_2C/MoS_2: one resulted from Nb-O contaminations at 531.3 eV[49], one from C-O contaminations at 532.5 eV[44], and one from OH surface termination groups at 533.7 eV[44]. These three components shifted to 530.0 eV, 531.4 eV, and 532.5 eV for pristine Nb_2C. It is worth noting that the ratio of the C-O component in Nb_2C/MoS_2 is significantly enhanced as compared to the pristine Nb_2C, demonstrating an increase of oxygen content at the surface of Nb_2C after the *in situ* growth of MoS_2 (Fig. 2(c) lower plane).

The Mo 3d peaks shown in Fig. S2 consist of four components. The main peaks located at 229.0 eV ($3d_{5/2}$) and 232.1 eV ($3d_{3/2}$) corresponds to the Mo-S bonding[50]. For the S element (Fig. 2(d)), the peaks located at 226.3 eV, 162.4 eV, and 161.2 eV were assigned to S 2s, S $2p_{1/2}$, and S $2p_{3/2}$, respectively[36]. Moreover, the peaks located at 168.4 eV were ascribed to the Nb-S bonding[46], indicating a strong combination of Nb_2C and MoS_2. Figure 2(e) shows the high-resolution XPS spectrum of F 1s, it can be seen that the -F surface termination was removed from the Nb_2C/MoS_2 heterostructure, which could be attributed to the F desorption during the heat treatment[51].

To determine the change of work function, the comparison of the XPS secondary electron cut-off (SEC) between Nb_2C and Nb_2C/MoS_2 was shown in Fig. 2(f). The SEC correspond to the position where the detected electron has the highest binding energy, which is usually combined with the position of the Fermi edge to determine the escape work of the material: $\phi_m = h\nu - E_{K,\,max}^{meas}$, where ϕ_m is the work function of sample, $h\nu$ and $E_{K,\,max}^{meas}$ are the photon energy and the detected highest binding energy in the SEC. The SEC energy of Nb_2C/MoS_2 is larger than that of Nb_2C. According to the basic principle of photoelectron spectroscopy[52,53], the work function of Nb_2C/MoS_2 is smaller than that of Nb_2C. In other words, *in situ* MoS_2 construction on the surface of Nb_2C can be used to tailor the work function of Nb_2C.

Figure 3 shows crystal models of Nb_2C with surface groups of -F, -O, and - OH[27], monolayer MoS_2, and Nb_2C/MoS_2 heterostructure used to investigate interface carrier-transfer and work function variations. The electrostatic potential of MoS_2 and Nb_2C monolayer with surface groups of -F, -O, and -OH, along the *z* direction (vertical plane), were shown in Fig. S3(a–d), respectively. The work function is defined as the energy required to extract an electron from the Fermi level to the surface of

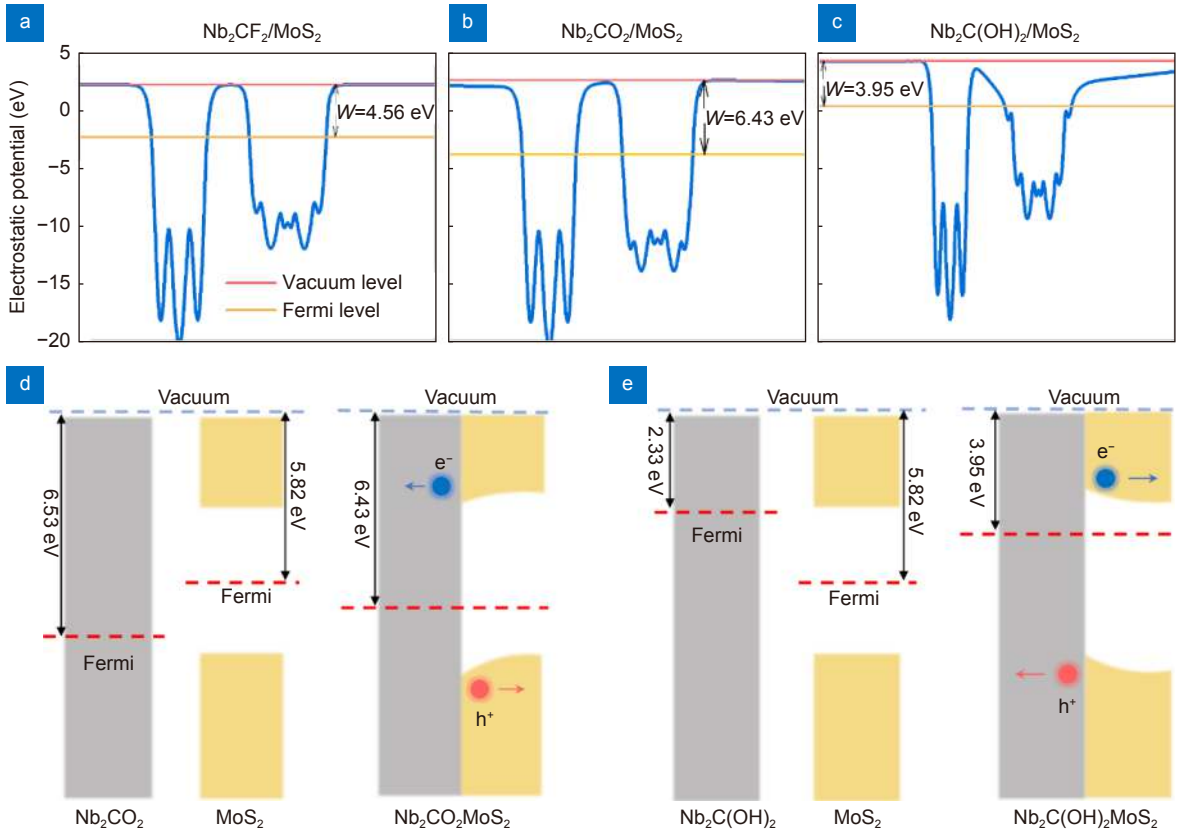

Fig. 3 | The calculated work functions of (**a**) Nb_2CF_2/MoS_2, (**b**) Nb_2CO_2/MoS_2, (**c**) $Nb_2C(OH)_2/MoS_2$. The charge-transfer and band alinement diagram of (**d**) Nb_2CO_2/MoS_2 and (**e**) $Nb_2C(OH)_2/MoS_2$.

a solid[54], which is equal to the energy difference between the vacuum level and Fermi level used in DFT calculation. Hence, the work function was determined to be 5.82 eV, 4.58 eV, 6.53 eV, and 2.33 eV for MoS_2, Nb_2CF_2, Nb_2CO_2, $Nb_2C(OH)_2$, respectively. Interestingly, the work function of Nb_2C MXene is very sensitive to its surface terminations: changing from O termination to OH termination causes the work function to decrease over 4 eV, which could be attributed to the variation of dipole moment density of MXene with different terminations[55]. The surface termination-dependent work function properties of MXene may provide a golden opportunity to modulate carrier behavior at the 2D heterostructure interface.

Figure 3(a–c) illustrated the work function of the interface of Nb_2CF_2/MoS_2, Nb_2CO_2/MoS_2, and $Nb_2C(OH)_2/MoS_2$, which give the work function of 4.56 eV, 6.43 eV, and 3.95 eV, respectively. The work function of heterostructures is different from its pristine compound due to charge redistribution and interface interaction. Moreover, the variation of surface terminations in Nb_2C also changes the work function of the heterostructure. As schematically shown in Fig. 3(d), the electron could transfer from MoS_2 to Nb_2CO_2 after the contact because the Fermi level of MoS_2 is higher than that of Nb_2CO_2, resulting in a decrease in work function in Nb_2CO_2 after contact. In contrast, the electron could transfer from $Nb_2C(OH)_2$ to MoS_2, resulting in the increase of work function in $Nb_2C(OH)_2$ after contact (Fig. 3(e)). When the XPS results in the valence band region are combined, we can conclude that the O termination dominated the surface group after the synthesis of heterostructures. We did not consider the Nb_2CF_2/MoS_2 situation because the XPS experiment results indicated F termination desorption during the synthesis process.

To analyze the effects of *in situ* growth of MoS_2 and surface group changes on linear optical properties of Nb_2C, the optical absorption properties of Nb_2C and Nb_2C/MoS_2 were investigated with UV-visible spectrometry combined with DFT calculation. As shown in Fig. 4(a), the strong broadband optical extinction was observed in the near-infrared (NIR) region having a peak at about 850 nm, which was recognized as the optical feature of Nb_2C MXenes[21]. Due to its good dispersibility in water, the absorbance of Nb_2C dispersion is proportional to its concentration. The extinction coefficient was

linearly fitted to be 16.13 L $cm^{-1}g^{-1}$ (Fig. S4) using the Beer-Lambert law. The DFT calculated optical absorption spectra with different terminations were shown in Fig. 4(b). Because the incident directions are random in dispersion during the UV-visible spectrometry, the calculated values of absorption are the average of three directions (*x*, *y*, and *z*). The difference between experimental and calculated results can be attributed to the termination and environment deviations. Even though the calculated results are not consistent with the experimental results, the average of three calculated spectrums (Nb_2CF_2, $Nb_2C(OH)_2$, and Nb_2CO_2) shows a similar tendency to the experimental results, which indicates that the experimentally synthesized Nb_2C naturally terminated with F, O, and OH. The enhancement in the near-infrared region can be observed in the average curve, which is inherited from Nb_2CF_2, indicating that the broadband optical extinction in the near-infrared region of Nb_2C in Fig. 4(a) was due to the F termination.

The experimentally obtained absorption spectra of Nb_2C, MoS_2, Nb_2C/MoS_2 were shown in Fig. 4(c) for comparison. We normalized the absorption coefficients of three spectra at 300 nm in Fig. 4(c) to highlight the significance of the three groups. The absorption peak of MoS_2 located in the range of 600–700 nm was attributed to the general features of MoS_2[56]. Furthermore, the absorption of MoS_2 increases sharply as the wavelength decreases below 800 nm, whereas the absorption of Nb_2C decreases. It appears that MoS_2 replenishes the Nb_2C absorption in the visible region, resulting in the increased absorption of Nb_2C/MoS_2 heterostructure in the visible region (450 nm – 800 nm). While the increased absorption of Nb_2C/MoS_2 in the NIR region (>800 nm) is inherited from Nb_2C. In other words, Nb_2C/MoS_2 inherited the preponderance of Nb_2C and MoS_2 in absorption, exhibiting broadband enhanced optical absorption. The DFT calculated spectra of MoS_2, Nb_2CO_2/MoS_2, and $Nb_2C(OH)_2/MoS_2$ shown in Fig. 4(d) are used to explore the mechanism of their outstanding absorption. The calculated MoS_2 spectra exhibited a similar absorption trend to the experimental results, but the peaks in the calculation spectrum show a blue shift when compared to the experimental spectrum. The blue shift could be ascribed to an underestimation of the band gap in the generalized gradient approximation (GGA) level during DFT calculation. Due to the F desorption during the heat

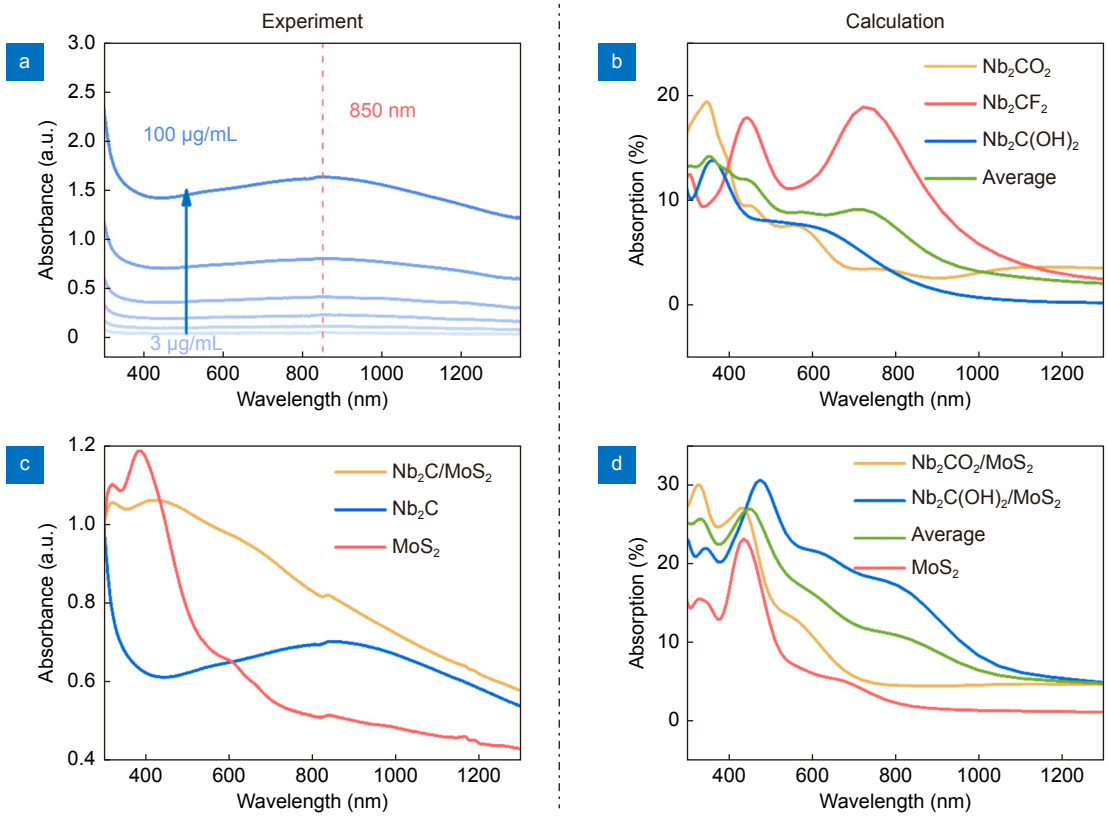

Fig. 4 | (**a**) UV-vis spectrum of Nb_2C solution with different concentrations. Inset: absorbance as a function of concentration. (**b**) DFT calculated absorption spectrum of Nb_2C with different terminations. (**c**) UV-vis spectrum of Nb_2C/MoS_2 solution. (**d**) DFT calculated absorption spectrum of Nb_2C/MoS_2 with different terminations.

treatment, we averaged the calculated spectra of Nb_2CO_2/MoS_2 and $Nb_2C(OH)_2/MoS_2$. The averaged line is more consistent with the measured Nb_2C/MoS_2 spectrum than the pristine Nb_2CO_2/MoS_2 and $Nb_2C(OH)_2/MoS_2$ absorption curves, manifesting that the O and OH groups are interacting with the surface of Nb_2C.

In order to further study the nonlinear optical properties of Nb_2C/MoS_2, the OA Z-scan technique was utilized to determine the NLO response of Nb_2C/MoS_2 and Nb_2C in the near-infrared region. The details of the measurement setup can be found in the experimental section. The OA Z-scan results of Nb_2C/MoS_2 and Nb_2C with the excitation wavelength of 1300 nm and 1550 nm are shown in Fig. 5(a) and 5(b), respectively. Both Nb_2C/MoS_2 and Nb_2C exhibit typical saturable absorption (SA), that is, the normalized transmittance increases as the sample approaches $z = z_0$ point. For the control of the NLO experiment, the linear transmittance of Nb_2C/MoS_2 and Nb_2C were set to be approximate consistency. Given this premise, the Nb_2C/MoS_2 exhibited a stronger SA response than that of the Nb_2C at the wavelength of 1300 nm and 1550 nm.

The intrinsic NLO absorption coefficient can be calculated by fitting the OA Z-scan results to the NLO theory. The NLO propagation equation can be written as[56]: $\frac{dI}{dz'} = -(\alpha_0 + \alpha_{NL} I)I$, where z' is the transmission

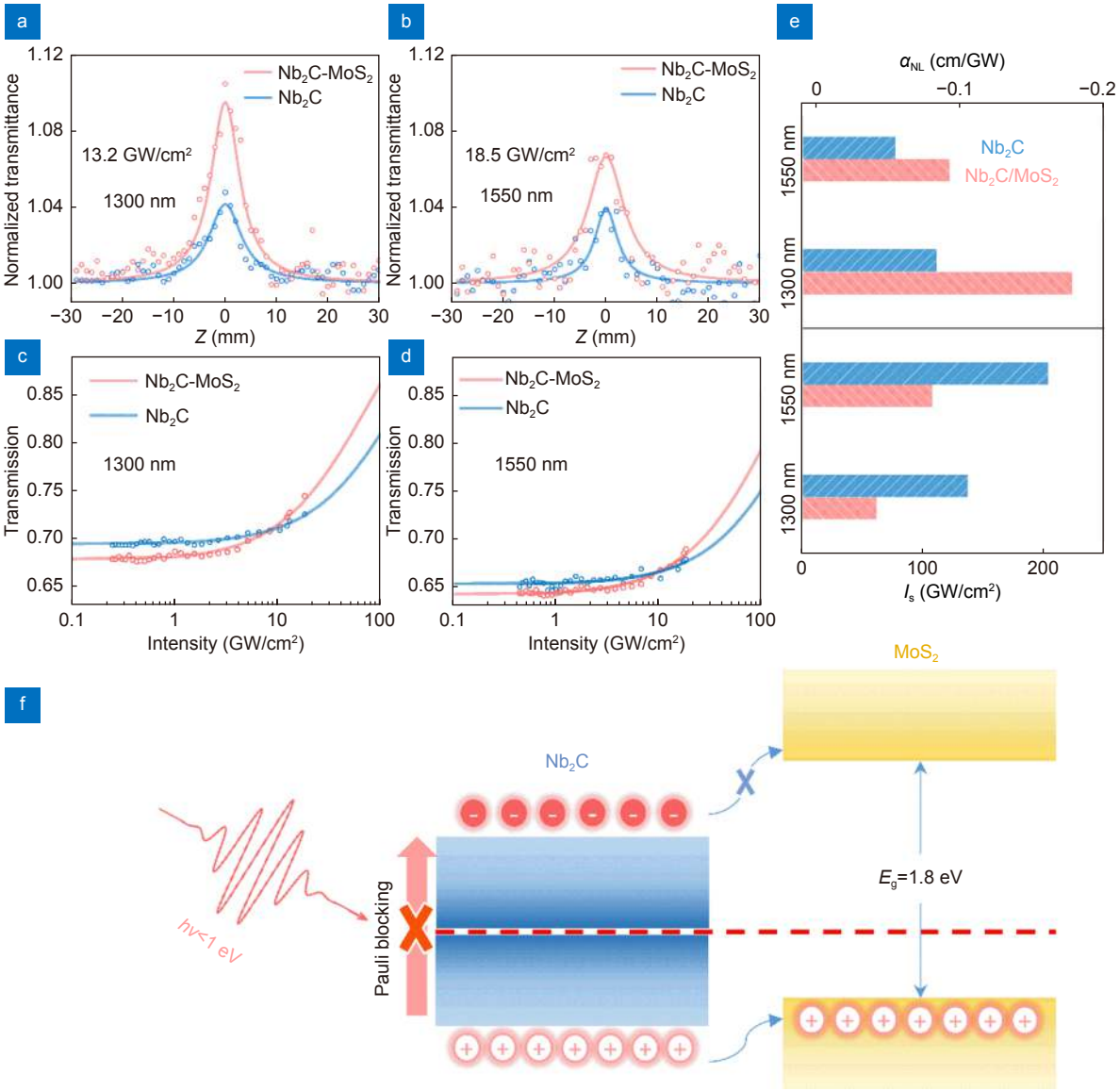

Fig. 5 | OA Z-scan results of Nb_2C/MoS_2 and Nb_2C with an excitation wavelength of (**a**) 1300 nm and (**b**) 1550 nm. The corresponding nonlinear transmittance curves under excitation optical intensity are shown in (**c**) and (**d**). (**e**) Histogram of I_s and α_{NL}. (**f**) Schematic diagram of the transfer process of photogenerated carriers and enhanced nonlinear absorption process in Nb_2C/MoS_2.

distance in the sample, α_0 and α_{NL} are the linear part and nonlinear part of the absorption coefficient, respectively. Giving the optical intensity $I_z = I_0/(1+z^2/z_0^2)$, where z is the position along the laser propagation direction, z_0 is the Rayleigh length and I_0 is the peak intensity on the axis, the NLO propagation can be solved as:

$$T = \frac{1}{\sqrt{\pi}q_0}\int_{-\infty}^{\infty}\ln[1+q_0\exp(-x^2)]\mathrm{d}x\ . \qquad (1)$$

To further assess the saturable absorption properties, a simplified saturable absorption model with a two-level system can be expressed as[57]:

$$T = \exp\left[-\left(\alpha_1 + \frac{\alpha_2}{1+I/I_s}\right)\right]\ , \qquad (2)$$

where T is transmission, α_1 is the non-saturable loss component, α_2 is modulation depth, and I_s is saturated intensity. Here, the Z-scan curves were converted into a function of transmission with optical intensity for fitting using the Eq. (2). The stand OA Z-scan model with Eq. (1) works very well for the curves in Fig. 5(a) and 5(b). The two-level system model with Eq. (2) also fits the converted traces well in Fig. 5(c) and 5(d). All the NLO fitting parameters are listed in Table 1.

As shown in Fig. 5(e), the NLO absorption coefficient α_{NL} of Nb_2C/MoS_2 was determined to be −0.18 cm/GW, and −0.09 cm/GW at 1300, and 1550 nm. For Nb_2C, these values are −0.08 cm/GW, and −0.05 cm/GW at 1300, and 1550 nm. As a comparison, α_{NL} of different 2D materials are shown in Fig. S6, indicating a comparable NLO performance of Nb_2C/MoS_2 with classical 2D materials. In addition, the saturated intensity I_s of Nb_2C/MoS_2 was fitted as 61.3 GW/cm², and 107.8 GW/cm² at 1300, and 1550 nm, respectively. While I_s of Nb_2C was estimated to be 136.9 GW/cm², and 203.2 GW/cm² at 1300, and 1550 nm, respectively. As expected, the α_{NL} of Nb_2C/MoS_2 is larger than that of Nb_2C at both 1300 and 1550 nm wavelengths, that is, Nb_2C/MoS_2 possesses a greater ability to alter absorption coefficient than the Nb_2C at the given optical intensity. In comparison, the fitted I_s shows opposite trend with α_{NL}: Nb_2C/MoS_2 had a lower saturated intensity than Nb_2C, and a shorter wavelength corresponding to a lower saturated intensity. Because I_s represents half of the optical intensity required for a complete bleaching of materials[58], implying that the Nb_2C/MoS_2 is more easily saturated than Nb_2C.

Key insight into the enhanced saturable absorption process of Nb_2C/MoS_2 was schematically shown in Fig. 5(f). The saturable absorption in the NIR region of Nb_2C/MoS_2 and Nb_2C can be attributed to the Pauli blocking induced by the intense single-photon transition. That is, the excited electrons gradually occupied possible states in the conduction band until all available states are full. After further increasing the incident light intensity, optical bleaching occurs according to Pauli blocking theory. Hence, the intensity of saturable absorption is naturally linked with the number of excited states[58,59]. In addition, the single photon transition mainly originated from Nb_2C instead of MoS_2, because the excitation photon energy (< 1 eV) is smaller than the band gap of MoS_2 (~1.8 eV)[34]. Moreover, the previous characterization, and calculation indicated that the surface group of Nb_2C/MoS_2 was dominated by O elements, implying that the Fermi level of Nb_2C/MoS_2 is close to the valence band of MoS_2 as presented in Fig. 3(d). Because the electron and hole can spontaneously transfer to energies closer to the Fermi level, the photon-excited holes in Nb_2C could transfer to MoS_2, whereas this process is prohibited for the electrons. On the one hand, saturable absorption is the process by which states gradually exhaust. On the other hand, MoS_2 offers the additional occupying state for carriers through the transfer process. Hence, Nb_2C/MoS_2 can offer more states to be exhausted, leading to a stronger and easier saturable absorption than the pristine Nb_2C.

Conclusions

In summary, we have observed the improved linear and nonlinear optical performance of an Nb_2C/MoS_2 heterostructure designed in this study. The XPS characterizing and work function calculation revealed that the dominated surface group of Nb_2C/MoS_2 was O termination,

Table 1 | Linear and nonlinear optical parameters of Nb_2C and Nb_2C/MoS_2.

Sample	λ (nm)	α_0 (cm^{-1})	α_{NL} (cm/GW)	Modulation depth α_2	I_s (GW/cm²)
Nb_2C/MoS_2	1300	3.68	−0.18	0.39	61.3
	1550	7.23	−0.09	0.45	107.8
Nb_2C	1300	3.68	−0.08	0.37	136.9
	1550	7.23	−0.05	0.43	203.2

leading to the decrease in the work function of Nb_2C after the *in situ* growth of MoS_2. Experiment and theoretical calculations revealed that the Nb_2C/MoS_2 heterostructure has broadband-enhanced optical absorption. Furthermore, the OA Z-scan results showed that Nb_2C/MoS_2 has better NLO performance than Nb_2C. The enhanced NLO performance is attributed to the hole transfer from Nb_2C to MoS_2. The 2D Nb_2C/MoS_2 heterostructure was proved to possess excellent nonlinear optical response, indicating that Nb_2C/MoS_2 can be applicated in the field of optoelectronics and ultrafast photonics, such as saturable absorbers, optical switches, and optical diodes. This facile strategy of *in situ* construction of the 2D Nb_2C/MoS_2 heterostructure provides guidance for achieving robust light modulation and paves the way for the development of broadband optoelectronic devices and optical modulators.

References

1. Novoselov KS, Geim AK, Morozov SV, Jiang D, Zhang Y et al. Electric field effect in atomically thin carbon films. *Science* **306**, 666–669 (2004).
2. Zeng C, Lu H, Mao D, Du YQ, Hua H et al. Graphene-empowered dynamic metasurfaces and metadevices. *Opto-Electron Adv* **5**, 200098 (2022).
3. Sun ZP, Martinez A, Wang F. Optical modulators with 2D layered materials. *Nat Photonics* **10**, 227–238 (2016).
4. Bonaccorso F, Sun Z, Hasan T, Ferrari AC. Graphene photonics and optoelectronics. *Nat Photonics* **4**, 611–622 (2010).
5. Chernikov A, Berkelbach TC, Hill HM, Rigosi A, Li YL et al. Exciton binding energy and nonhydrogenic Rydberg series in monolayer WS_2. *Phys Rev Lett* **113**, 076802 (2014).
6. Wang YW, Deng ZL, Hu DJ, Yuan J, Ou QD et al. Atomically thin noble metal dichalcogenides for phase-regulated meta-optics. *Nano Lett* **20**, 7811–7818 (2020).
7. Elbanna A, Chaykun K, Lekina Y, Liu YD, Febriansyah B et al. Perovskite-transition metal dichalcogenides heterostructures: recent advances and future perspectives. *Opto-Electron Sci* **1**, 220006 (2022).
8. Zhang GW, Huang SY, Wang FJ, Xing QX, Song CY et al. The optical conductivity of few-layer black phosphorus by infrared spectroscopy. *Nat Commun* **11**, 1847 (2020).
9. Wang ZT, Xu YH, Dhanabalan SC, Sophia J, Zhao CJ et al. Black phosphorus quantum dots as an efficient saturable absorber for bound soliton operation in an erbium doped fiber laser. *IEEE Photonics J* **8**, 1503310 (2016).
10. Wu LM, Huang WC, Wang YZ, Zhao JL, Ma DT et al. 2D tellurium based high-performance all-optical nonlinear photonic devices. *Adv Funct Mater* **29**, 1806346 (2019).
11. Wu LM, Dong YZ, Zhao JL, Ma DT, Huang WC et al. Kerr nonlinearity in 2D graphdiyne for passive photonic diodes. *Adv Mater* **31**, 1807981 (2019).
12. Xie ZJ, Zhang F, Liang ZM, Fan TJ, Li ZJ et al. Revealing of the ultrafast third-order nonlinear optical response and enabled photonic application in two-dimensional tin sulfide. *Photonics Res* **7**, 494–502 (2019).
13. Ren J, Lin H, Zheng XR, Lei WW, Liu D et al. Giant and light modifiable third-order optical nonlinearity in a free-standing h-BN film. *Opto-Electron Sci* **1**, 210013 (2022).
14. Wang YW, Zhou L, Zhong MZ, Liu YP, Xiao S et al. Two-dimensional noble transition-metal dichalcogenides for nanophotonics and optoelectronics: Status and prospects. *Nano Res* **15**, 3675–3694 (2022).
15. Wang YW, Liu S, Zeng BW, Huang H, Xiao J et al. Ultraviolet saturable absorption and ultrafast carrier dynamics in ultrasmall black phosphorus quantum dots. *Nanoscale* **9**, 4683–4690 (2017).
16. Wei H, Wang YD, Wang YW, Fan WX, Zhou L et al. Giant two-photon absorption in MXene quantum dots. *Opt Express* **30**, 8482–8493 (2022).
17. Wu LM, Fan TJ, Wei SR, Xu YJ, Zhang Y et al. All-optical logic devices based on black arsenic–phosphorus with strong nonlinear optical response and high stability. *Opto-Electron Adv* **5**, 200046 (2022).
18. Naguib M, Kurtoglu M, Presser V, Lu J, Niu JJ et al. Two-dimensional nanocrystals produced by exfoliation of Ti_3AlC_2. *Adv Mater* **23**, 4248–4253 (2011).
19. Frey NC, Wang J, Bellido GIV, Anasori B, Gogotsi Y et al. Prediction of synthesis of 2D metal carbides and nitrides (MXenes) and their precursors with positive and unlabeled machine learning. *ACS Nano* **13**, 3031–3041 (2019).
20. VahidMohammadi A, Rosen J, Gogotsi Y. The world of two-dimensional carbides and nitrides (MXenes). *Science* **372**, eabf1581 (2021).
21. Maleski K, Shuck CE, Fafarman AT, Gogotsi Y. The broad chromatic range of two-dimensional transition metal carbides. *Adv Opt Mater* **9**, 2001563 (2021).
22. Han MK, Maleski K, Shuck CE, Yang YZ, Glazar JT et al. Tailoring electronic and optical properties of MXenes through forming solid solutions. *J Am Chem Soc* **142**, 19110–19118 (2020).
23. Sharbirin AS, Akhtar S, Kim J. Light-emitting MXene quantum dots. *Opto-Electron Adv* **4**, 200077 (2021).
24. Lin H, Wang YW, Gao SS, Chen Y, Shi JL. Theranostic 2D tantalum carbide (MXene). *Adv Mater* **30**, 1703284 (2018).
25. Agresti A, Pazniak A, Pescetelli S, Di Vito A, Rossi D et al. Titanium-carbide MXenes for work function and interface engineering in perovskite solar cells. *Nat Mater* **18**, 1228–1234 (2019).
26. Dong YC, Chertopalov S, Maleski K, Anasori B, Hu LY et al. Saturable absorption in 2D Ti_3C_2 MXene thin films for passive photonic diodes. *Adv Mater* **30**, 1705714 (2018).
27. Wang YD, Wang YW, Chen KQ, Qi K, Xue TY et al. Niobium carbide MXenes with broad-band nonlinear optical response and ultrafast carrier dynamics. *ACS Nano* **14**, 10492–10502 (2020).
28. Li H, Chen SY, Boukhvalov DW, Yu ZY, Humphrey MG et al. Switching the nonlinear optical absorption of titanium carbide MXene by modulation of the surface terminations. *ACS Nano* **16**, 394–404 (2022).
29. Wang Y, Wang Y, He J. 2D Transition Metal Carbides (MXenes) for Third Order Nonlinear Optics: Status and Prospects. Laser Photonics Rev 2023, 2200733. https://doi.org/10.1002/lpor.202200733
30. Liu Y, Weiss NO, Duan XD, Cheng HC, Huang Y et al. Van der Waals heterostructures and devices. *Nat Rev Mater* **1**, 16042

(2016).
31. Li ZW, Yang W, Huang M, Yang X, Zhu CG et al. Light-triggered interfacial charge transfer and enhanced photodetection in CdSe/ZnS quantum dots/MoS2 mixed-dimensional phototransistors. *Opto-Electron Adv* **4**, 210017 (2021).
32. Chen JY, Eul T, Lyu L, Li YL, Hu XY et al. Tracing the formation of oxygen vacancies at the conductive LaAlO3/SrTiO3 interface via photoemission. *Opto-Electron Sci* **1**, 210011 (2022).
33. Tagliabue G, DuChene JS, Abdellah M, Habib A, Gosztola DJ et al. Ultrafast hot-hole injection modifies hot-electron dynamics in Au/p-GaN heterostructures. *Nat Mater* **19**, 1312–1318 (2020).
34. Conley HJ, Wang B, Ziegler JI, Haglund RF Jr, Pantelides ST et al. Bandgap engineering of strained monolayer and bilayer MoS_2. *Nano Lett* **13**, 3626–3630 (2013).
35. Ma K, Jiang H, Hu Y, Li C. 2D nanospace confined synthesis of pseudocapacitance-dominated MoS_2-in-Ti_3C_2 superstructure for ultrafast and Stable Li/Na-ion batteries. *Adv Funct Mater* **28**, 1804306 (2018).
36. Yuan ZY, Wang LL, Li DD, Cao JM, Han W. Carbon-reinforced Nb_2CT_x MXene/MoS_2 nanosheets as a superior rate and high-capacity anode for sodium-ion batteries. *ACS Nano* **15**, 7439–7450 (2021).
37. Wang X, Li H, Li H, Lin S, Ding W et al. 2D/2D 1T-MoS_2/Ti_3C_2 MXene heterostructure with excellent supercapacitor performance. *Adv Funct Mater* **30**, 0190302 (2020).
38. Kohn W, Sham LJ. Self-consistent equations including exchange and correlation effects. *Phys Rev* **140**, A1133–A1138 (1965).
39. Wang V, Xu N, Liu JC, Tang G, Geng WT. VASPKIT: a user-friendly interface facilitating high-throughput computing and analysis using VASP code. *Comput Phys Commun* **267**, 108033 (2021).
40. Wang YD, Wang YW, Dong YL, Zhou L, Wei H et al. The nonlinear optical transition bleaching in tellurene. *Nanoscale* **13**, 15882–15890 (2021).
41. Luo Y, Cheng C, Chen HJ, Liu K, Zhou XL. Systematic investigations of the electron, phonon and elastic properties of monolayer M_2C (M = V, Nb, Ta) by first-principles calculations. *J Phys Condens Matter* **31**, 405703 (2019).
42. Lin H, Gao SS, Dai C, Chen Y, Shi JL. A two-dimensional biodegradable niobium carbide (MXene) for photothermal tumor eradication in NIR-I and NIR-II biowindows. *J Am Chem Soc* **139**, 16235–16247 (2017).
43. Geng XM, Zhang YL, Han Y, Li JX, Yang L et al. Two-dimensional water-coupled metallic MoS_2 with nanochannels for ultrafast supercapacitors. *Nano Lett* **17**, 1825–1832 (2017).
44. Shen CJ, Wang LB, Zhou AG, Wang B, Wang XL et al. Synthesis and electrochemical properties of two-dimensional RGO/$Ti_3C_2T_x$ nanocomposites. *Nanomaterials* **8**, 80 (2018).
45. Schultz T, Frey NC, Hantanasirisakul K, Park S, May SJ et al. Surface termination dependent work function and electronic properties of $Ti_3C_2T_x$ MXene. *Chem Mater* **31**, 6590–6597 (2019).
46. Zong H, Hu L, Gong SJ, Yu K, Zhu ZQ. Flower-petal-like Nb_2C MXene combined with MoS_2 as bifunctional catalysts towards enhanced lithium-sulfur batteries and hydrogen evolution. *Electrochim Acta* **404**, 139781 (2022).
47. Halim J, Cook KM, Naguib M, Eklund P, Gogotsi Y et al. X-ray photoelectron spectroscopy of select multi-layered transition metal carbides (MXenes). *Appl Surf Sci* **362**, 406–417 (2016).
48. Darlinski A, Halbritter J. Angle-resolved XPS studies of oxides at NbN, NbC, and Nb surfaces. *Surf Interface Anal* **10**, 223–237 (1987).
49. Sarma DD, Rao CNR. XPES studies of oxides of second- and third-row transition metals including rare earths. *J Electron Spectrosc Relat Phenom* **20**, 25–45 (1980).
50. Woo HC, Nam IS, Lee JS, Chung JS, Lee KH et al. Room-temperature oxidation of $K_2CO_3MoS_2$ catalysts and its effects on alcohol synthesis from CO and H_2. *J Catal* **138**, 525–535 (1992).
51. El-Demellawi JK, Lopatin S, Yin J, Mohammed OF, Alshareef HN. Tunable multipolar surface plasmons in 2D $Ti_3C_2T_x$ MXene flakes. *ACS Nano* **12**, 8485–8493 (2018).
52. Helander MG, Greiner MT, Wang ZB, Lu ZH. Pitfalls in measuring work function using photoelectron spectroscopy. *Appl Surf Sci* **256**, 2602–2605 (2010).
53. Helander MG, Greiner MT, Wang ZB, Tang WM, Lu ZH. Work function of fluorine doped tin oxide. *J Vac Sci Technol A* **29**, 011019 (2011).
54. Kahn A. Fermi level, work function and vacuum level. *Mater Horiz* **3**, 7–10 (2016).
55. Liu YY, Xiao H, Goddard III WA. Schottky-barrier-free contacts with two-dimensional semiconductors by surface-engineered MXenes. *J Am Chem Soc* **138**, 15853–15856 (2016).
56. Wang KP, Wang J, Fan JT, Lotya M, O'Neill A et al. Ultrafast saturable absorption of two-dimensional MoS_2 nanosheets. *ACS Nano* **7**, 9260–9267 (2013).
57. Jiang XT, Liu SX, Liang WY, Luo SJ, He ZL et al. Broadband nonlinear photonics in few-layer MXene $Ti_3C_2T_x$ (T = F, O, or OH). *Laser Photon Rev* **12**, 1700229 (2018).
58. Bao QL, Zhang H, Wang Y, Ni ZH, Yan YL et al. Atomic-layer graphene as a saturable absorber for ultrafast pulsed lasers. *Adv Funct Mater* **19**, 3077–3083 (2009).
59. Breusing M, Kuehn S, Winzer T, Malić E, Milde F et al. Ultrafast nonequilibrium carrier dynamics in a single graphene layer. *Phys Rev B* **83**, 153410 (2011).

Acknowledgements

The authors are grateful for the financial support from the National Natural Science Foundation of China (Nos. 61874141, 11904239), Natural Science Foundation of Hunan Province (Grant Nos. 2021JJ40709, 2021JJ20080, 2022JJ20080), Postgraduate Innovative Project of Central South University (Grant No. 2021zzts0056), Open Sharing Found for the Large-scale Instruments and Equipment of Central South University. This work was supported in part by the High Performance Computing Center of Central South University.

Author contributions

All authors commented on the manuscript.

Competing interests

The authors declare no competing financial interests.

Supplementary information

The Supplementary information is available at https://doi.org/10.29026/oea.2023.220162